九州大学学術情報リポジトリ
Kyushu University Institutional Repository

Temperature dependence of the yield stress in TiZrNbHfTa body-centred cubic high-entropy alloy

Tanaka, Masaki
Department of Materials, Faculty of Engineering, Kyushu University

Yamasaki, Shigeto
Department of Materials, Faculty of Engineering, Kyushu University

Morikawa, Tatsuya
Department of Materials, Faculty of Engineering, Kyushu University

https://hdl.handle.net/2324/7169370

出版情報：Materials Science and Engineering A. 871, pp.144917-, 2023-04-26. Elsevier
バージョン：
権利関係：Creative Commons Attribution International

KYUSHU UNIVERSITY

Materials Science & Engineering A 871 (2023) 144917

Contents lists available at ScienceDirect

Materials Science & Engineering A

journal homepage: www.elsevier.com/locate/msea

Temperature dependence of the yield stress in TiZrNbHfTa body-centred cubic high-entropy alloy

Masaki Tanaka *, Shigeto Yamasaki, Tatsuya Morikawa

Department of Materials, Faculty of Engineering, Kyushu University, 744 Motooka, Nishi-ku, Fukuoka, 819-0395, Japan

ARTICLE INFO

Keywords:
Stress/stain measurements
Metallic alloys
Plasticity
Characterisation
Fracture behaviour

ABSTRACT

Body-centred cubic (bcc) high-entropy alloys exhibit high strength. However, their yield behaviour and controlling mechanisms are still ambiguous. In this study, the temperature dependence of the yield stress, effective stress, activation volume, and activation enthalpy in a polycrystalline bcc refractory high-entropy alloy of TiZrNbHfTa were measured by tensile tests at 77–750 K. At temperatures above 650 K, the temperature dependence of the yield stress disappeared, and serration appeared in stress–strain curves. By extrapolating the effective shear stress to 0 K, the Peierls stress was estimated to be 580 MPa. The value was compared with different crystals using the relationship $\frac{\tau_p}{\mu}$ and $\frac{h}{b}$, where τ_p is the Peierls stress, μ is the shear modulus, h is the distance between the slip planes, and b is the Burgers vector. The $\frac{\tau_p}{\mu}$ value in this study was slightly higher than that of other bcc crystals. The activation enthalpy below 260 K corresponds to that of other bcc crystals with high Peierls potentials, suggesting kink-pair nucleation is the controlling mechanism of the dislocation glide in this temperature range. Meanwhile, the activation enthalpy above 260 K deviated from the trendline, indicating the changes in the dislocation glide from the kink-pair nucleation to other one.

1. Introduction

Body-centred cubic (bcc) crystals show strong temperature dependence. In particular, the critical resolved shear or yield stress of pure-iron single crystals or polycrystals is one order larger at 77 K than those at room temperature [1–3]. As bcc crystals have a high Peierls potential, the dislocation glide in iron is a thermally activated process. In the low-temperature range where the yield stress is temperature-dependent, the magnitude of the yield stress is controlled by the dislocation velocity, that is, the frequency of forming a kink-pair along a screw dislocation controls the yield stress. When the temperature decreases, the frequency of a kink-pair decreases. As a result, the applied stress should be increased at the temperature to maintain the dislocation velocity to fulfil the applied strain rate, thereby increasing the yield stress. If the yield stress exceeds the fracture stress, the specimen cannot undergo plastic deformation and fractures in a brittle manner.

High-entropy alloys have garnered attention. In these alloys, several crystal structures are noted, such as face-centred cubic (fcc), bcc, B2, A2, hexagonal close-packed (hcp), and a combination of these phases [4–13]. As there is no dominant element in the crystal, the mechanism of plastic deformation, particularly the behaviour of the dislocation motion, remains ambiguous.

Bcc high-entropy alloys are considered as refractory alloys owing to their high strength at high temperatures [13–30]. In particular, TiZrNbHfTa exhibits good deformability at high temperatures [14], which can be attributed to its suppressed intergranular fracture. In terms of yield stress, single-crystalline TiZrNbHfTa shows abnormally high yield stress at 873 K, which does not appear in polycrystalline materials, owing to the dynamic strain precipitation [20]. Because the yield behaviour and the controlling mechanisms of these alloys themselves are still ambiguous, it is essential to unveil the deformation mechanism in bcc high-entropy alloy in the first place.

In this study, the yield stress and activation volume of TiZrNbHfTa high-entropy alloys were measured using tensile tests over a wide temperature range (77–750 K). It is to be noted that tensile tests have rarely been performed in this alloy. Subsequently, the activation enthalpy for the dislocation glide was measured. Then, the controlling mechanism of the dislocation glide at low temperatures is discussed, at which the elementary process of the dislocation glide stands out.

* Corresponding author.
E-mail address: masaki@zaiko.kyushu-u.ac.jp (M. Tanaka).

https://doi.org/10.1016/j.msea.2023.144917
Received 5 January 2023; Received in revised form 4 March 2023; Accepted 13 March 2023
Available online 15 March 2023
0921-5093/© 2023 The Authors. Published by Elsevier B.V. This is an open access article under the CC BY license (http://creativecommons.org/licenses/by/4.0/).

2. Experimental

A bcc TiZrNbHfTa high-entropy alloy with an isotonic ratio was used. An ingot was obtained by arch melting. The width and length of the parallel portion of the specimen were set to 2 and 8 mm, respectively. The initial strain rate was set to 4.2×10^{-4} s^{-1}. The thickness of each specimen was 1 mm. A strain gauge was attached at the centre of the parallel portion. Strain rate jump tests were performed, in which the strain rate was increased by a factor of 10 at a strain of approximately 0.01 during each tensile test. The mechanical tests were performed between 77 K and 750 K. The temperatures below room temperature were controlled by cold gas evaporating liquid nitrogen, and the temperatures above room temperature were controlled in an image furnace. The temperature was stabilised within 2°.

3. Results

Fig. 1 (a) shows an inverse pole figure map with respect to the normal direction of a bcc TiZrNbHfTa high-entropy alloy, showing equiaxial grains and the average equivalent diameter of the grains was approximately 230 μm. Fig. 1 (b) shows pole figures with respect to the normal direction taken from the area shown in (a) on a stereo projection and a standard triangle, indicating that there is a slightly stronger distribution of the grains facing {110} planes to the normal direction. As the texture is not strong, its effect on the mechanical property is considered to be negligible. Fig. 1 (c) shows the elemental maps of Ti, Zr, Nb, Hf, and Ta obtained by energy-dispersive X-ray microscopy. No precipitates or segregations were noted. The temperature dependence of 0.2% proof stress was measured at 77–750 K. Fig. 2 shows the nominal stress–nominal strain (s–s) curves of the specimen at 200–750 K. Yield stress decreases with increasing temperature except for that at 750 K. The work hardening rate decreases with increasing temperature below 550 K. Because the work hardening is strongly influenced by the cross slip of dislocations, the difference in the work hardening among temperatures should be attributed to the change in the frequency of cross slipping with the temperature above and below 550 K. The s–s curves obtained at 650 and 750 K show serration during plastic deformation. At 650 K, the specimen fractured during work hardening with the reduction of the ductility due to dynamic strain ageing. The increase in the strain hardening at 650 K and 750 K is attributed to the dynamic strain ageing.

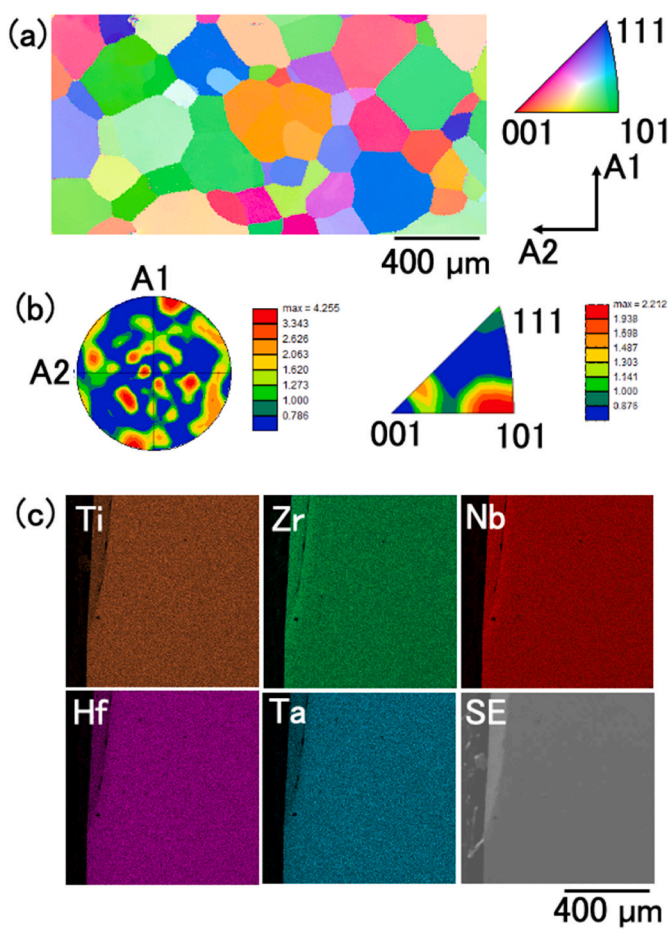

Fig. 1. (a) Inverse pole figure map with respect to the normal direction of bcc TiZrNbHfTa high-entropy alloy. (b) Pole figures with respect of the normal direction taken from the area shown in (a) with a stereographic projection and a standard triangle. The directions of A1 and A2 are sown in (a). (c) Energy-dispersive spectroscopy maps and secondary electron image of the investigated area of the specimen. The length scales of (a) and (c) are identical.

Fig. 3(a)–(d) show scanning electron microscopy (SEM) images of the fracture surfaces at 77, 200, 296, and 650 K, respectively. Intergranular fractures were mainly noted in the specimen fractured at 77 K. Meanwhile, intergranular and ductile fracture surfaces were observed in the specimens fractured at 200 and 296 K. Fully ductile fracture surfaces were observed in the specimen fractured at 650 K. The intergranular fracture reduces the ductility in the tensile tests at below 296 K.

Fig. 4(a) shows the temperature dependence of the 0.2% proof stress. The strong temperature dependence of the proof stress is similar to that of other bcc crystals [2,31–34]. The proof stress, $\sigma_{0.2}(T)$, is divided into two components: the effective stress, σ_e (T), which is temperature-dependent, and athermal stress, σ_{ath}, which is temperature-independent, as follows:

$$\sigma_{0.2}(T) = \sigma_e(T) + \sigma_{ath}. \quad (1)$$

In this study, the athermal stress was obtained as 655 MPa, which is the average proof stress when the temperature dependence nearly disappears above 650 K. Using the Taylor factor as $M = 2$ [35], the effective shear stress is given as follows:

$$\tau_e(T) = \frac{\sigma_{0.2}(T) - \sigma_{ath}}{M}. \quad (2)$$

Fig. 4(b) shows the temperature dependence of the effective shear stress with a regression curve, omitting the data plots from the specimen which fractured in a brittle manner before yielding. By extrapolating the regression curve to 0 K, the Peierls stress was estimated to be 580 MPa.

As plastic deformation is the result of dislocation motion, primitive process of the dislocation motion should be investigated. The tempera-

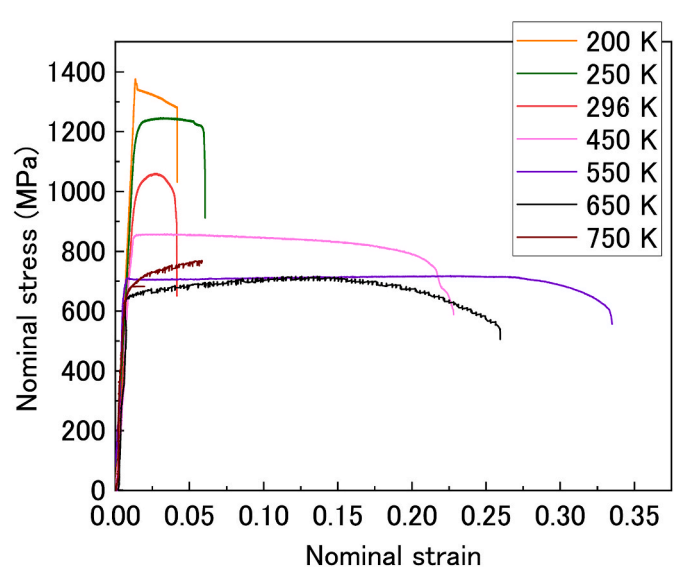

Fig. 2. Stress–strain curves of bcc TiZrNbHfTa high-entropy alloy.

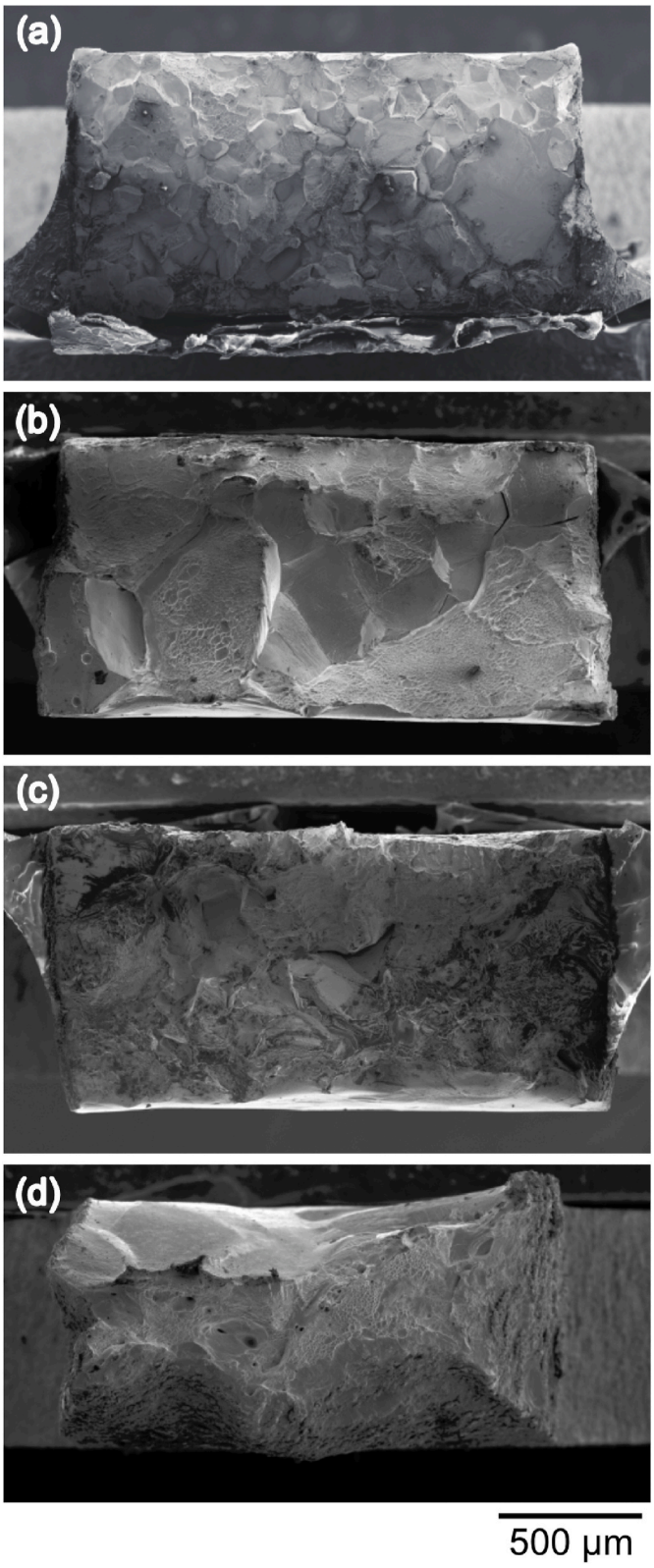

Fig. 3. SEM images of the fracture surfaces of bcc TiZrNbHfTa high-entropy alloy at (a) 77 K, (b) 200 K, (c) 296 K, and (d) 650 K. The magnifications of the figures are the same, where a common scale bar is put on the right bottom of the figure.

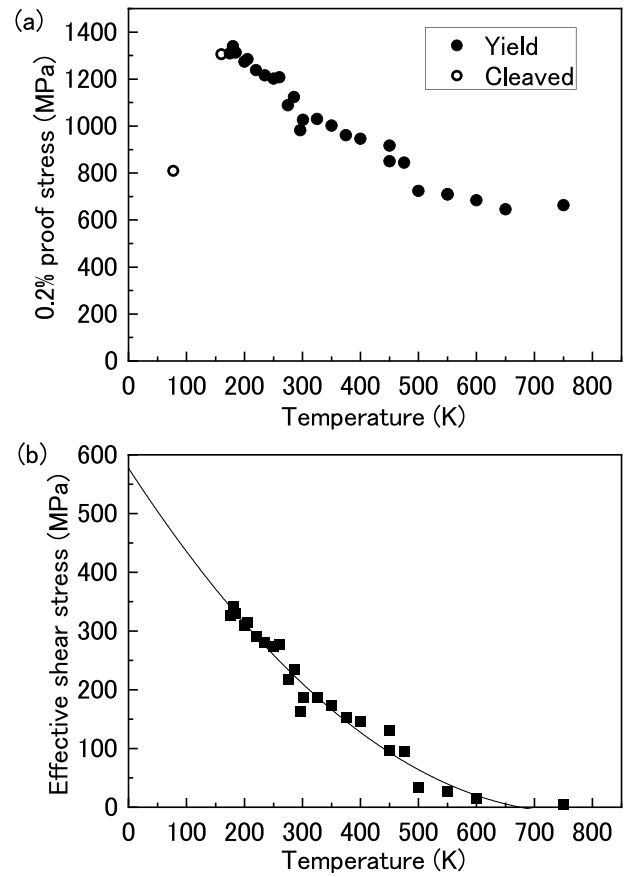

Fig. 4. (a) Temperature dependence of the yield stress. The solid symbols indicate that the specimen yielded, whereas the open symbols indicate that the specimen fractured in a brittle manner before yielding. (b) Temperature dependence of the effective shear stress. The data of the brittle fracture before yielding were omitted.

ture dependence of the activation volume was obtained. Strain jump tests were performed to obtain the value of activation volume V^*. When the tensile strain rate jumped to $\dot{\varepsilon}_2$ from $\dot{\varepsilon}_1$, the applied stress changed to σ_2 from σ_1. The activation volume is then obtained as follows:

$$V^* = kTM\frac{\ln\left(\frac{\dot{\varepsilon}_2}{\dot{\varepsilon}_1}\right)}{\sigma_2(T) - \sigma_1(T)}, \tag{3}$$

where k is the Boltzmann's constant. In this study, the strain rate was increased by a factor of 10.

Fig. 5 shows the temperature dependence of the activation volume, where the left vertical axis is normalised to the cube of the Burgers vector. The value of the Burgers vector was calculated as $\frac{a\sqrt{3}}{2}$ where $a = 0.34 \times 10^{-9}$ m [14]. The value at 300 K is consistent with the value obtained in previous studies [36,37]. The activation volume increased with the temperature as the trend. At low temperatures below 250 K the value is close to those for kink-pair nucleation [38]. At approximately 600 K, where the value of the effective stress decreased to 0, the activation volume abruptly increased. The activation volume of more than 100 b^3 is close to the lowest value when mobile dislocations interact with the forest dislocations [39]. In addition to that, the inverse temperature dependence of the activation volume appeared at approximately 300 K. The abnormality of the temperature dependence of the activation volume will briefly be discussed later in the discussion section.

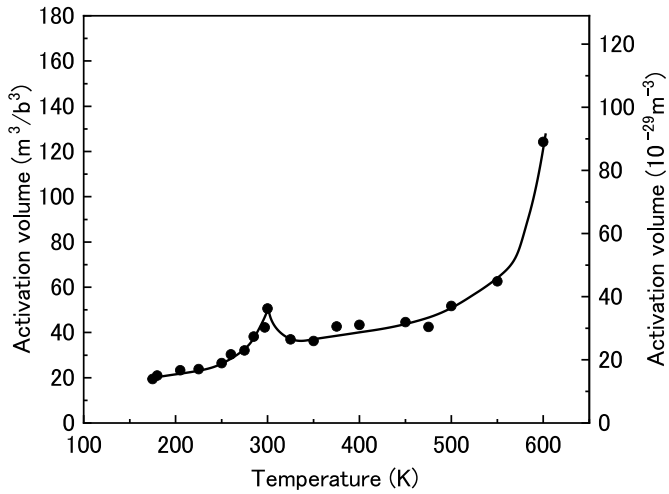

Fig. 5. Temperature dependence of the activation volume. The left vertical axis is normalised with the cube of the Burgers vector.

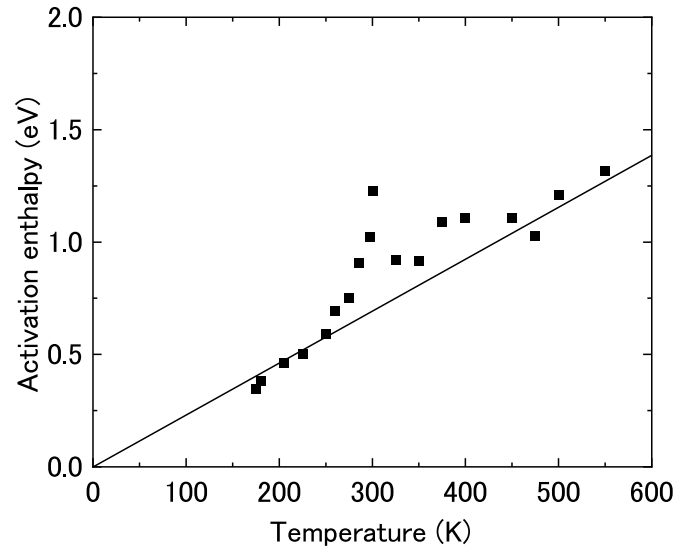

Fig. 6. Temperature dependence of the activation enthalpy of bcc TiZrNbHfTa high-entropy alloy. The solid line is drawn with the slope of 28 kT intersecting with the origin.

4. Discussion

There are two points to be discussed in this session. One is the abnormal temperature dependence of activation volume, and the other is the controlling mechanism of yield stress at low temperatures. First, the abnormal temperature dependence of activation volume seen in Fig. 5 is discussed.

The abnormal temperature dependence of the activation volume shown in Fig. 5 has also been reported for Ti and other alloys [40–47]. In particular, this can be ascribed to the interaction of the dislocations with the oxygen or hydrogen atoms during dynamic strain ageing [41]. Another suggested mechanism is the two rate-controlling processes governing the dislocation motion in this temperature range [44]. Anne et al. [47] showed that the dominant slip system activated in Ti–6Al–4V changed from basal to pyramidal around the temperature at which the activation volume exhibits an inverse temperature dependence. In-situ transmission electron microscopy (TEM) observation in iron showed jerky dislocation motion at the temperature range of dynamic strain ageing [48]. It suggests that such atoms that induce dynamic strain ageing influence the primitive process of dislocation glide. Therefore, it is presumed that the inverse temperature dependence of the activation volume in the high-entropy alloy used in this study is also ascribed to the change in the controlling mechanism either dynamic strain ageing or change in slip mode, or both in the temperature range; however, further analysis is necessary.

Next, the controlling mechanism for yield stress at low temperatures is discussed. Here, the temperature dependence of the activation enthalpy for the dislocation glide was first obtained to discuss the nature of dislocation glide, comparing the obtained Peierls stress of TiZrNbHfTa with those of other pure crystals. Subsequently, the process of dislocation glide in the bcc high-entropy alloy used in this study was explained.

Here, the activation enthalpy is given by Refs. [49,50]:

$$H^* = -TV^*\frac{\partial \tau_e}{\partial T}. \tag{4}$$

The slope of H^* with respect to temperature is approximately 20–30 kT [51–53], whereby the dislocation motion is governed by the Peierls mechanism, and the kink-pair formation is the controlling mechanism for the dislocation glide. Fig. 6 shows the experimentally obtained temperature dependence of H^* in this study. A straight-line intersecting with the origin has a slope of 28 kT. Several data plots at T < 260 K are on along the line, whereas the date deviated from the line at 260 K ≦ T, whereby the activation volume showed an abnormal temperature dependence, as shown in Fig. 5. This indicates that the controlling mechanism for the dislocation glide differs at temperatures below and above 260 K. In particular, below 260 K, as the slope of the plots is close to 28 kT, the dominant dislocation process is considered to be the kink-pair nucleation at high Peierls potentials as those in other bcc crystals. Above 260 K, the change in the activation enthalpy suggests that the controlling process of dislocation glide changes from the kink-pair nucleation.

In-situ TEM observations of the bcc high-entropy alloys indicate that edge dislocations contribute to plastic deformation [54]. The TEM observations also noted that the dislocation segments move and are dynamically pinned. However, it was suggested that the dominant process of dislocation glide is the motion of screw dislocations at room temperature. Meanwhile, the contribution of the edge dislocations increased with temperature. It is speculated that the changes in the activation enthalpy and the activation volume above 260 K are correlated with the change in the activated component from screw dislocations to edge dislocations. Anyhow, even though the high-entropy alloy with five atoms of equivalent ratios was used in this study, the dislocation glide below 260 K is controlled by the Peierls mechanism, similar to other bcc crystals.

The magnitude of the Peierls stress was estimated next. The Peierls stress τ_p, is given by [55]

$$\frac{\tau_p}{\mu} = Aexp\left(-B \bullet \frac{h}{b}\right), \tag{5}$$

where μ is the shear modulus, A and B are constants including the Poisson's ratio, h is the distance between the slip planes, and b is Burgers vector.

Fig. 7 shows the relationship between $\frac{\tau_p}{\mu}$ and $\frac{h}{b}$ in pure single crystals [56]. Even with difference in the crystals of the same structures, the Peierls stress exhibits an exponential function $\frac{h}{b}$. The $\frac{h}{b}$ and $\frac{\tau_p}{\mu}$ values of the bcc crystals were approximately 0.8 and 6×10^{-3}, respectively. The τ_p value, which corresponds to the stress at 0 K, was estimated to be 580 MPa by extrapolating the effective shear stress (Fig. 4(b)), at which the shear modulus at 0 K for TiZrNbHfTa was estimated as follows [18]:

$$\mu(T) = 36.2 - \frac{5.6}{\left(exp\left(\frac{845}{T}\right) - 1\right)}\ [\text{GPa}]. \tag{6}$$

The plots from the specimen used in this study also overlap in Fig. 7,

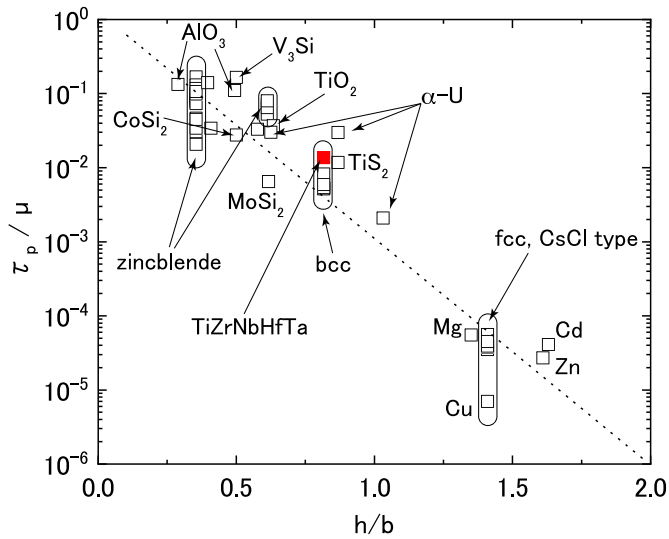

Fig. 7. Relationship between $\frac{\tau_p}{\mu}$ and $\frac{h}{b}$ in various single crystals [56]. The result obtained in this study is plotted as red solid square. (For interpretation of the references to colour in this figure legend, the reader is referred to the Web version of this article.)

showing that $\frac{\tau_p}{\mu}$ is 0.0136 which is slightly higher than those for other bcc pure crystals as seen in the figure.

One of the questions arises here is that why the Peierls stress was higher than that of other pure bcc alloys. In other words, it is a question that either the interaction of dislocations with solute atoms or high Peierls potential controls the yield stress at low temperatures in bcc high-entropy alloys. Note here that τ_p obtained in this study is not strictly the Peierls stress, but the stress required to move a screw dislocation at 0 K.

The yield stress in pure fcc and hcp crystals has weak temperature dependence because of the low Peierls stress. Therefore, the temperature dependence of the yield stress in their alloys is ascribed to the solute atoms, that is, the interaction of the dislocations and solute atoms controls yield stress. Meanwhile, in crystals with a high Peierls potential, such as bcc crystals, the temperature dependence of the yield stress is governed by the frequency of kink-pair nucleation. Solute atoms in bcc crystals often decrease the yield stress at *low temperatures*,[1] which is called solution softening [2,31,57–62]. Therefore, the interaction of solute atoms and dislocations at low temperatures is expected not to increase the yield stress also in high-entropy alloys. Maresca and Curtin [63] suggested a cross-kink mechanism to explain the high strength of bcc high-entropy alloys. In their model, kinked structures are formed at local sites where statistical fluctuations occur with the local solute configurations along a screw dislocation without stress. When stress is applied, kink pairs are formed along the screw dislocations on different slip planes. These cross kinks move along the screw dislocations and interact to extinguish each other, thereby forming vacancies or interstitial atom. These defects interact with other mobile dislocations to increase the stress required for the dislocations to move. This strengthening mechanism does not violate the results obtained in this study. The temperature dependence for plastic deformation below 260 K can be explained by kink-pair nucleation, which induces strong temperature dependence in this temperature range.

[1] Solute atoms induce solid solution hardening in the temperature range where the effective stress is much smaller than the Peierls stress. The effect of solution hardening becomes apparent around room temperatures for iron, for example.

5. Conclusion

The temperature dependence of the yield stress, effective stress, activation volume, and activation enthalpy were measured in a polycrystalline bcc refractory high-entropy alloy of TiZrNbHfTa using tensile tests at 77–750 K. The following findings were obtained:

1) The yield stress decreases with increasing temperature. The temperature dependence of the yield stress disappeared above 650 K. Moreover, the athermal stress of TiZrNbHfTa used in this study was 655 MPa.
2) The effective shear stress at 0 K was estimated to be 580 MPa by extrapolating the curve of effective shear stress versus temperature.
3) $\frac{\tau_p}{\mu}$ was obtained as 6×10^{-3}, which is slightly higher than that for other bcc pure single crystals.
4) The temperature dependence of the activation volume below 260 K was close to that of the materials for a high Peierls potential. The activation volume exhibited an abnormal temperature dependence at approximately 300 K.
5) The activation enthalpy below 250 K are in good agreement with those obtained from other bcc materials with high Peierls potentials, suggesting that the controlling mechanism for yielding is kink-pair nucleation along screw dislocations.

This work experimentally showed that the temperature dependence of the yield stress below 250 K is ascribed to the motion of the screw dislocations, which is similar to that of other bcc crystals. Further, the controlling mechanism changed as the temperature increased, which can be attributed to the increased contribution of the edge dislocations as temperature increased, however, further investigation is necessary.

Funding

This work was supported by the JSPS KAKENHI (Grant-in-Aid for Scientific Research on Innovative Areas) [grant number JP18H05451].

Data statement

Data will be made available on request.

CRediT authorship contribution statement

Masaki Tanaka: Conceptualization, Methodology, Writing – original draft, Funding acquisition. **Shigeto Yamasaki:** Validation, Writing – review & editing. **Tatsuya Morikawa:** Validation, Methodology, Writing – review & editing.

Declaration of competing interest

The authors declare that they have no known competing financial interests or personal relationships that could have appeared to influence the work reported in this paper.

Data availability

Data will be made available on request.

Acknowledgement

The authors thank Mrs Y. Shinozaki for the assistance during the experiment.

References

[1] D. Brunner, J. Diehl, Strain-rate and temperature-dependence of the tensile flow-stress of high-purity alpha-iron above 250-K (Regime I) studied by means of stress-

relaxation tests, Phys. Status Solidi 124 (1991) 155–170, https://doi.org/10.1002/pssa.2211240114.
[2] M. Tanaka, K. Matsuo, N. Yoshimura, G. Shigesato, M. Hoshino, K. Ushioda, K. Higashida, Effects of Ni and Mn on brittle-to-ductile transition in ultralow-carbon steels, Mater. Sci. Eng., A 682 (2017) 370–375, https://doi.org/10.1016/j.msea.2016.11.045.
[3] E. Kuramoto, Y. Aono, K. Kitajima, S. Mater, Thermally activated slip deformation of high-purity iron single-crystals between 4.2K and 300K, Scripta Metall. 13 (1979) 1039–1042, https://doi.org/10.1016/0036-9748(79)90199-6.
[4] J.W. Yeh, S.K. Chen, S.J. Lin, J.Y. Gan, T.S. Chin, T.T. Shun, C.H. Tsau, S.Y. Chang, Nanostructured high-entropy alloys with multiple principal elements: novel alloy design concepts and outcomes, Adv. Eng. Mater. 6 (2004) 299–303, https://doi.org/10.1002/adem.200300567.
[5] B. Cantor, I.T.H. Chang, P. Knight, A.J.B. Vincent, Microstructural development in equiatomic multicomponent alloys, Mater. Sci. Eng., A 375–377 (2004) 213–218, https://doi.org/10.1016/j.msea.2003.10.257.
[6] D.B. Miracle, M.-H. Tsai, O.N. Senkov, V. Soni, R. Banerjee, Refractory high entropy superalloys (RSAs), Scripta Mater. 187 (2020) 445–452, https://doi.org/10.1016/j.scriptamat.2020.06.048.
[7] Y.F. Ye, Q. Wang, J. Lu, C.T. Liu, Y. Yang, High-entropy alloy: challenges and prospects, Mater. Today 19 (2016) 349–362, https://doi.org/10.1016/j.mattod.2015.11.026.
[8] D.B. Miracle, O.N. Senkov, A critical review of high entropy alloys and related concepts, Acta Mater. 122 (2017) 448–511, https://doi.org/10.1016/j.actamat.2016.08.081.
[9] H.Y. Diao, R. Feng, K.A. Dahmen, P.K. Liaw, Fundamental deformation behavior in high-entropy alloys: an overview, Curr. Opin. Solid State Mater. Sci. 21 (2017) 252–266, https://doi.org/10.1016/j.cossms.2017.08.003.
[10] J. Shi, Y.Z. Zhang, X. Wang, C.L. Jiang, M. Wang, C. Ma, H. Huang, Microstructure and mechanical properties of UNbTiHf1-xMox high-entropy alloys, Mater. Sci. Eng., A 860 (2022), 144239, https://doi.org/10.1016/j.msea.2022.144239.
[11] H. Ren, R.R. Chen, X.F. Gao, T. Liu, G. Qin, S.P. Wu, J.J. Guo, Phase formation and mechanical features in (AlCoCrFeNi)100-Hf high-entropy alloys: the role of Hf, Mater. Sci. Eng., A 858 (2022), 144156, https://doi.org/10.1016/j.msea.2022.144156.
[12] H. Inui, K. Kishida, Z. Chen, Recent progress in our understanding of phase stability, atomic structures and mechanical and functional properties of high-entropy alloys, Mater. Trans. 63 (2022) 394–401, https://doi.org/10.2320/matertrans.MT-M2021234.
[13] Q. Wang, J. Han, Y. Liu, Z. Zhang, C. Dong, P.K. Liaw, Coherent precipitation and stability of cuboidal nanoparticles in body-centered-cubic Al0.4Nb0.5Ta0.5TiZr0.8 refractory high entropy alloy, Scripta Mater. 190 (2021) 40–45, https://doi.org/10.1016/j.scriptamat.2020.08.029.
[14] O.N. Senkov, J.M. Scott, S.V. Senkova, D.B. Miracle, C.F. Woodward, Microstructure and room temperature properties of a high-entropy TaNbHfZrTi alloy, J. Alloys Compd. 509 (2011) 6043–6048, https://doi.org/10.1016/j.jallcom.2011.02.171.
[15] O.N. Senkov, C. Woodward, D.B. Miracle, Microstructure and properties of aluminum-containing refractory hiigh-entropy alloys, JOM 66 (2014) 2030–2042, https://doi.org/10.1007/s11837-014-1066-0.
[16] W. Wu, S. Ni, Y. Liu, M. Song, Effects of cold rolling and subsequent annealing on the microstructure of a HfNbTaTiZr high-entropy alloy, J. Mater. Res. 31 (2016), https://doi.org/10.1557/jmr.2016.445, 3815-2823.
[17] N.D. Stepanov, N.Y. Yurchenko, S.V. Zherebtsov, M.A. Tikhonovsky, G. A. Salishchev, Aging behavior of the HfNbTaTiZr high entropy alloy, Mater. Lett. 211 (2018), https://doi.org/10.1016/j.matlet.2017.09.094, 87-90.
[18] G. Laplanche, P. Gadaud, L. Perrière, I. Guillot, J.P. Couzinié, Temperature dependence of elastic moduli in a refractory HfNbTaTiZr high-entropy alloy, J. Alloys Compd. 799 (2019) 538–545, https://doi.org/10.1016/j.jallcom.2019.05.322.
[19] X. Yang, Y. Zhang, P.K. Liaw, Microstructure and compressive properties of NbTiVTaAlx high entropy alloys, Proceedia Eng 36 (2012) 292–298, https://doi.org/10.1016/j.proeng.2012.03.043.
[20] H.Y. Yasuda, Y. Yamada, K. Cho, T. Nagase, Deformation behavior of HfNbTaTiZr high entropy alloy singe crystals and polycrystals, Mater. Sci. Eng., A 809 (2021), 140983, https://doi.org/10.1016/j.msea.2021.140983.
[21] K. Ren, H. Liu, R. Chen, Y. Tang, B. Guo, S. Li, J. Wang, R. Wang, F. Lu, Compression properties and impact energy release characteristics of TiZrNbV high-entropy alloy, Mater. Sci. Eng., A 827 (2021), 142074, https://doi.org/10.1016/j.msea.2021.142074.
[22] Z. Han, L. Meng, J. Yang, G. Liu, J. Yang, R. Wei, G. Zhang, Novel BCC VNbTa refractory multi-element alloys with superior tensile properties, Mater. Sci. Eng., A 825 (2021), 141908, https://doi.org/10.1016/j.msea.2021.141908.
[23] M. Wang, Z.L. Ma, Z.Q. Xu, X.W. Cheng, Effects of vanadium concentration on mechanical properties of VxNbMoTa refractory high-entropy alloys, Mater. Sci. Eng., A 808 (2021), 140848, https://doi.org/10.1016/j.msea.2021.140848.
[24] Q. Liu, G. Wang, Y. Liu, X. Sui, Y. Chen, S. Luo, Hot deformation behaviors of an ultrafine-grained MoNbTaTiV refractory high-entropy alloy fabricated by powder metallurgy, Mater. Sci. Eng., A 809 (2021), 140922, https://doi.org/10.1016/j.msea.2021.140922.
[25] L.L. Ma, X.W. Li, B.R. Sun, S.W. Xin, T.D. Shen, Low activation V–Fe–Cr–Mn high-entropy alloys with exceptional strength, Mater. Sci. Eng., A 860 (2022), 144243, https://doi.org/10.1016/j.msea.2022.144243.
[26] Q. Wei, A. Zhang, J. Han, B. Xin, B. Su, X. Wang, J. Meng, A novel Hf30Nb25Ta25Ti15Mo5 refractory high entropy alloy with excellent combination of strength and ductility, Mater. Sci. Eng., A 857 (2022), 144035, https://doi.org/10.1016/j.msea.2022.144035.
[27] Z. Li, W. Lai, X. Tong, D. You, W. Li, X. Wang, Design of TiZrNbTa multi-principal element alloys with outstanding mechanical properties and wear resistance, Mater. Sci. Eng., A 845 (2022), 143203, https://doi.org/10.1016/j.msea.2022.143203.
[28] X. Wang, L. Wang, T. Li, K. Jin, B. Wang, Y. Li, S. Sun, Y. Xue, Precipitation enhancing strain hardening capability of ductile AlTiVZrNb high-entropy alloys upon dynamic loading, Mater. Sci. Eng., A 856 (2022), 143964, https://doi.org/10.1016/j.msea.2022.143964.
[29] W. Li, K. Xiong, L. Yang, S. Zhang, J. He, Y. Wang, Y. Mao, An ambient ductile TiHfVNbTa refractory high-entropy alloy: cold rolling, mechanical properties, lattice distortion, and first-principles prediction, Mater. Sci. Eng., A 856 (2022), 144046, https://doi.org/10.1016/j.msea.2022.144046.
[30] S.H. Chen, J.S. Zhang, S. Guan, T. Li, J.Q. Liu, F.F. Wu, Y.C. Wu, Microstructure and mechanical properties of WNbMoTaZrx (x=0.1, 0.3 0.5, 1.0) refractory high entropy alloys, Mater. Sci. Eng., A 835 (2022), 142701, https://doi.org/10.1016/j.msea.2022.142701.
[31] J.R. Stephens, W.R. Witzke, Alloy softening in binary iron solid solutions, J. Less Common. Met. 48 (1976) 285–308, https://doi.org/10.1016/0022-5088(76)90009-6.
[32] H.W. Schadler, Mobility of edge dislocations on {110} planes in tungsten single crsytals, Acta Metall. 12 (1964) 681–870, https://doi.org/10.1016/0001-6160(64)90144-0.
[33] C.T. Wang, D.W. Bainbridge, Deformation mechanism for high-purity vanadium at low-temperatures, Metall. Trans. A 3 (1972) 3161–3165, https://doi.org/10.1007/BF02661327.
[34] Y. Aono, E. Kuramoto, K. Kitajima, Plastic deformation of high-purity iron single crystals, Rep. Res. Inst. Appl. Mech, Kyushu Univ. XXIX (1981) 127.
[35] M.J. Marcinkowski, H.A. Lipsitt, The plastic deformation of chromium at low temperatures, Acta Metall. 10 (1962) 95–111, https://doi.org/10.1016/0001-6160(62)90055-X.
[36] J.P. Couzinié, L. Lilensten, Y. Champion, G. Dirras, L. Perrière, I. Guillot, On the room temperature deformation mechanisms of a TiZrHfNbTa refractory high-entropy alloy, Mater. Sci. Eng., A 645 (2015) 255–263255, https://doi.org/10.1016/j.msea.2015.08.024.
[37] R.R. Eleti, N. Stepanov, N. Yurchenko, D. Klimenko, S. Zherebtsov, Plastic deformation of solid-solution strengthened Hf-Nb-Ta-Ti-Zr body-centered cubic medium/high-entropy alloys, Scripta Mater. 200 (2021), 113927, https://doi.org/10.1016/j.scriptamat.2021.113927.
[38] E. Kuramoto, Y. Aono, K. Kitajima, K. Maeda, S. Takeuchi, Thermally activated slip deformation between 0.7 and 77 K in high-purity iron single crsytals, Philos. Mag. A 39 (1979) 717–724, https://doi.org/10.1080/01418617908239302.
[39] T. Zhu, J. Li, A. Samanta, H.G. Kim, S. Suresh, Interfacial plasticity governs strain rate sensitivity and ductility in nanostructured metals, Proc. Natl. Acad. Sci. USA (2007) 3031–3036, https://doi.org/10.1073/pnas.0611097104.
[40] P. Soo, H. Higgins, The deformation of zirconium-oxygen single crystals, Acta Metall. 16 (1968) 177–186, https://doi.org/10.1016/0001-6160(68)90113-2.
[41] S.N. Moneiro, A.T. Santhanam, R.E. Reed-Hill, Athermal plastic deformation in commercial purity titanium, in: R.I. Jaffee, N.E. Promisel (Eds.), The Science, Technology and Application of Titanium, Pergamon Press, Oxford, London, Edinburgh, New York, Tronto, Sydney, Paris, Braunschweig, 1970, pp. 503–516.
[42] C. Brehm, P. Lehr, Etude dynamique du glissement prismatique dans le cas de monocristaux de titane, Mem. Sci. Rev. Metallurg. 68 (1971) 277–285.
[43] T. Tanaka, H. Conrad, Deformation kinetic for {1010}<1120> slip in titanium single crystals below $0.4T_m$, Acta Metall. 20 (1972) 1019–1029, https://doi.org/10.1016/0001-6160(72)90136-8.
[44] A. Akhtar, E. Teghtsoonian, Prismatic slip in alpha-titanium single crystals, Metall. Mater. Trans. A 6 (1975) 2201–2208, https://doi.org/10.1007/BF02818644.
[45] B.R. Anne, M. Tanaka, T. Morikawa, Temperature dependence of activation enthalpy for yielding in bimodal Ti–6Al–4V, Mater. Trans. 60 (2019) 1828–1832, https://doi.org/matertrans.ME201902.
[46] M. Tanaka, Y. Hayashi, Y. Okuyama, T. Morikawa, K. Higashida, Change in slip mode with temperature in Ti-0.49 mass%O, Mater. Trans. 60 (2019) 80–85, https://doi.org/10.2320/matertrans.M2018251.
[47] B.R. Anne, Y. Okuyama, T. Morikawa, M. Tanaka, Activated slip systems in bimodal Ti–6Al–4V plastically deformed at low and moderately high temperatures, Mater. Sci. Eng., A 798 (2020), 1402118, https://doi.org/10.1016/j.msea.2020.140211.
[48] D. Caillard, An in situ study of hardening and softening of iron by carbon interstitials, Acta Mater. 59 (2011) 4974–4989, https://doi.org/10.1016/j.actamat.2011.04.048.
[49] B.d. Meester, C. Yin, M. Doner, H. Conrad, Thermally activated deformation of crystalline solids, in: J.C.M. Li, A.K. Mukherjee (Eds.), Rate Processes in Plastic Deformation of Materials : Proceedings from the John E. Dorn Symposium, ASM, Ohio, USA, 1975, p. 175.
[50] H. Conrad, Effect of interstitial solutes on the strength and ductility of Titanium, Prog. Mater. Sci. 26 (1981) 123–403, https://doi.org/10.1016/0079-6425(81)90001-3.
[51] Y. Aono, K. Kitajima, E. Kuramoto, Thermall actived slip deformation of Fe-Ni alloy single-crystals in the temperature-range of 4.2K to 300K, Scripta Metall. 15 (1981) 275–279, https://doi.org/10.1016/0036-9748(81)90344-6.
[52] Z.S. Basinski, M.S. Duesbery, G.S. Murty, The orientation and temperature dependence of plastic flow in potassium, Acta Metall. 29 (1981) 807, https://doi.org/10.1016/0001-6160(81)90122-X, 807.

[53] M. Tanaka, K. Higashida, Temperature dependence of effective stress in severely deformed ultralow-carbon steel, Philos. Mag. A 96 (2016) 1979–1992, https://doi.org/10.1080/14786435.2016.1183828.
[54] F. Mompiou, D. Tingaud, Y. Chang, B. Gault, G. Dirras, Conventional vs harmonic-structured β-Ti-25Nb-25Zr alloys: a comparative study of deformation mechanisms, Acta Mater. 161 (2018) 420–430, https://doi.org/10.1016/j.actamat.2018.09.032.
[55] H.B. Huntington, Modification of the Peierls-Nabarro model for edge dislocation core, Proc. Phys. Soc. B 68 (1955) 1043–1048, https://doi.org/10.1088/0370-1301/68/12/308.
[56] Y. Kamimura, K. Edagawa, S. Takeuchi, Experimental evaluation of the Peielrs stresses in a variety of crystals and their relation to the crystal structure, Acta Mater. 61 (2013) 294–309, https://doi.org/10.1016/j.actamat.2012.09.059.
[57] W.A. Spitzig, W.C. Leslie, Solid-solution softening and thermally activated flow in alloys of Fe with 3 at.% Co, Ni or Si, Acta Metall. 19 (1971) 1143–1153, https://doi.org/10.1016/0001-6160(71)90046-0.
[58] K. Okazaki, Solid-solution hardening and softening in binary iron alloys, J. Mater. Sci. 31 (1996) 1087–1099, https://doi.org/10.1007/BF00352911.
[59] J. Syarif, T. Tsuchiyama, S. Takaki, Mechanism of toughening in ferritic iron by solute copper at low temperature, ISIJ Int. 43 (2003) 1100–1104, https://doi.org/10.2355/isijinternational.43.1100.
[60] K. Maeno, M. Tanaka, N. Yoshimura, H. Shirahata, K. Ushioda, K. Higashida, Change in dislocation mobility with Ni content in ferritic steels and its effect on brittle-to-ductile transition, Tetsu-To-Hagane 98 (2012) 667–674, https://doi.org/10.2355/tetsutohagane.98.667.
[61] M. Tanaka, D. Izumi, N. Yoshimura, G. Shigesato, M. Hoshino, K. Ushioda, K. Higashida, Temperature dependence of activation volume on Cu content of ultralow-carbon steel, Philos. Mag. A 97 (2017) 2915–2930, https://doi.org/10.1080/14786435.2017.1359423.
[62] T. Mohri, Y. Chen, M. Kohyama, S. Ogata, A. Saengdeejing, S.K. Bhattacharya, M. Wakeda, S. Shinzato, H. Kimizuka, Mechanical properties of Fe-rich Si alloy from Hamiltonian, NPJ Comput. Mater. 3 (2017) 10, https://doi.org/10.1038/s41524-017-0012-4.
[63] F. Maresca, W.A. Curtin, Mechanistic origin of high strength in refractory BCC high entropy alloys up to 1900K, Acta Mater. 182 (2020) 235–249, https://doi.org/10.1016/j.actamat.2019.10.015.